Metal–germanium–metal ultrafast infrared detectors

D. Buca, S. Winnerl, S. Lenk, S. Mantl, and Ch. Buchal[a)]
Institut für Schichten und Grenzflächen, ISG1-IT, Forschungszentrum Jülich, D-52425 Jülich, Germany

(Received 13 June 2002; accepted 18 September 2002)

We demonstrate silicon-based ultrafast metal–semiconductor–metal (MSM) photodetectors for near infrared optocommunication wavelengths. They show a response time of 12.5 ps full width at half maximum (FWHM) at both 1300 and 1550 nm wavelengths. The overall external quantum efficiencies are 13% at 1320 nm and 7.5% at 1550 nm. The sensitive volumes are 270 nm thick Ge films, grown on Si(111) by molecular beam epitaxy. Interdigitated Cr metal top electrodes with 1.5–5 μm spacing and identical finger width form Schottky contacts to the Ge film. A Ti-sapphire femtosecond laser with an optical parametric oscillator and an electro-optic sampling system are used to evaluate the temporal response, which is limited by the transit time of the carriers between electrodes. In addition, results on Si–Ge MSM heterostructure detectors with plate capacitor geometry are presented. At 1550 nm an ultrafast response of 9.4 ps FWHM and an overall quantum efficiency of 0.9% are measured.
[DOI: 10.1063/1.1519958]

I. INTRODUCTION

The integration of silicon microelectronics and optocommunications at standard wavelengths of 1300 and 1550 nm is an active field of research and development.[1] In the field of detectors, metal–semiconductor–metal (MSM) detectors play an important role because of their high sensitivity-bandwidth product, their fast response, and their ease of fabrication. Fast MSM photodetectors fall into two categories: fast response due to enhanced carrier recombination (short carrier lifetimes) or fast carrier collection due to a short transit time to the electrodes. In the first case, the semiconductor is heavily damaged or doped to obtain a high density of recombination centers, but strongly doped or even disordered material limits the carrier mobility and lowers the quantum efficiency. The MSM interdigitated design is easily adapted to these devices. Previous work focused mainly on GaAs and InGaAs heterostructures,[2] with only very few reports being presented for crystalline Si (Ref. 3) or Ge (Ref. 4). However, the development of epitaxial cobalt disilicide and its compatibility with crystalline Si has permitted a change from interdigitated electrodes to a vertical plate capacitor design with submicrometer drift lengths and optimum carrier saturation mobility. At present, the fastest electrical response from a MSM detector based on crystalline Si is 14 ps for the interdigitated electrode design,[3] but 3.2 ps for the vertical plate capacitor geometry.[5] Due to the use of crystalline Si, these detectors work well at $\lambda \leqslant 1.1\ \mu$m, but the quantum efficiency drops quickly at longer wavelengths. The internal photoeffect at Si–metal Schottky barriers is suitable for infrared (IR) detection, but it is of low efficiency. For IR absorption at $\lambda \leqslant 1.5\ \mu$m pure crystalline Ge is a suitable material. In this article, we demonstrate devices using high quality epitaxial Ge films integrated on silicon.

The epitaxial growth of high quality Ge on Si has been demonstrated before. Recently good quality Ge films on Si(111) were grown by chemical vapor deposition (CVD) using a low temperature deposited Ge buffer layer[6] and by molecular beam epitaxy (MBE) by surfactant mediated epitaxy (SME).[7]

Due to the lattice mismatch between Si and Ge, the growth of Ge on Si rapidly leads to island formation (Stransky–Krastanov growth mode with a critical thickness of about 1 nm). Thicker films relax from the formation of a dislocation network with defect densities of up to 10^{12} cm^{-2}.[8] It has been shown that on Si(111) island formation can be suppressed by using Sb as a surfactant. During the MBE process, Sb floats on the surface and reduces the mobility of the Ge atoms.[9]

We have grown Ge films of high crystalline quality using SME. A sufficiently low Sb doping concentration of 4×10^{16} cm^{-3} was achieved. This allows the formation of good Schottky contacts for Ge–MSM detectors. The detectors were excited by femtosecond pulses from a Ti–sapphire laser and an attached optical parametric oscillator (OPO) that provided the pump signal. The ultrafast electrical response was measured by an electro-optical sampling probe.

II. EXPERIMENTS AND RESULTS

A. Germanium film growth

High resistivity Si(111) wafers ($\rho > 1000\ \Omega$ cm) were prepared by a standard RCA cleaning procedure, omitting the final HF dip. The wafers were loaded into a MBE chamber with a base pressure of 2×10^{-11} mbar. The MBE system is equipped with electron beam evaporators for the deposition of Si and Ge and an effusion cell for Sb. The oxide formed by the last cleaning step was removed by heating the wafers to 800 °C for 30 min while providing a small flux of Si. Subsequently a 50 nm thick Si buffer layer was grown at a substrate temperature of 650 °C. Their reflection high energy

a)Electronic mail: c.buchal@fz-juelich.de

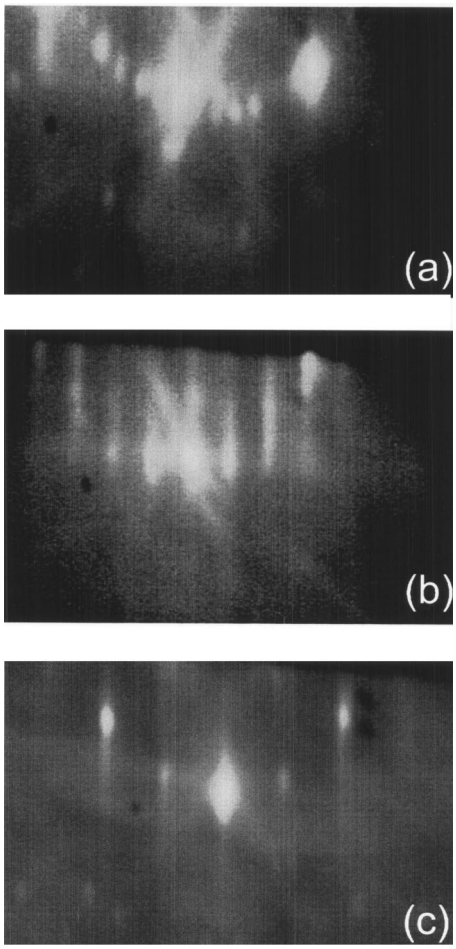

FIG. 1. RHEED patterns after different process steps. Si(111) with 7×7 reconstruction after buffer growth (a), $\sqrt{3}\times\sqrt{3}R30°$ reconstructed surface after coverage with a Sb monolayer (b), and a 2×1 reconstructed Sb terminated Ge surface after Ge film deposition.

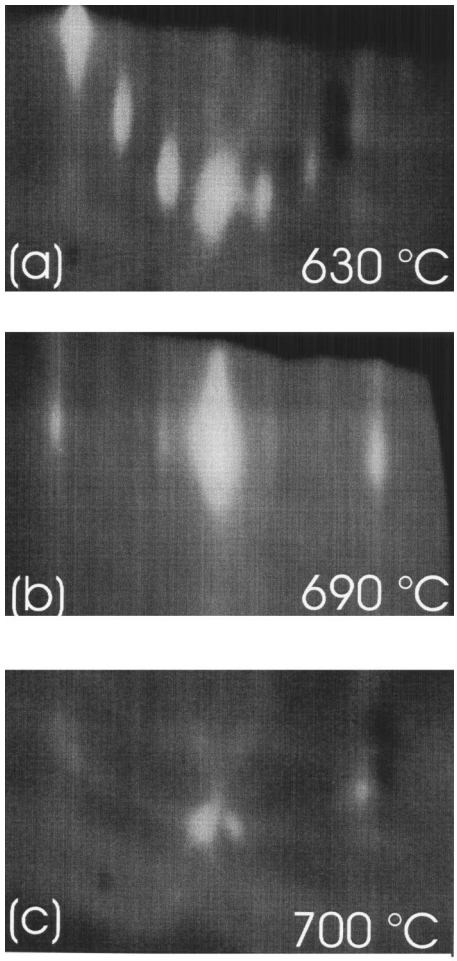

FIG. 2. RHEED patterns indicating different Sb coverage of the Si(111) surface at different substrate temperatures.

electron diffraction (RHEED) pattern was spotlike and contained reflexes corresponding to a 7×7 reconstructed surface [Fig. 1(a)]. Subsequently the surface was covered with a monolayer of Sb, which was confirmed by the occurrence of $\sqrt{3}\times\sqrt{3}$ $R30°$ reconstruction [Fig. 1(b)]. Finally a 300 nm thick Ge layer was grown at a Ge deposition rate of 70 pm/s while additional Sb was provided. The spotlike 2×1 reconstructed RHEED pattern of the germanium layer after deposition indicated a flat, Sb terminated surface [Fig. 1(c)]. The samples were grown at various substrate temperatures in the range from 600 to 710 °C. At higher temperatures, it was increasingly difficult to achieve sufficient Sb coverage of the Si surface due to the enhanced desorption of Sb. The RHEED patterns depicted in Fig. 2 illustrate this. In Fig. 2(a) spotlike strong reflexes from the $\sqrt{3}\times\sqrt{3}$ $R30°$ reconstruction indicate full Sb coverage of the Si surface with Sb temperature of 630 °C. The weaker streaklike peaks depicted in Fig. 2(b) indicate only partial Sb coverage at 690 °C. For 700 °C, no $\sqrt{3}\times\sqrt{3}$ $R30°$ reconstruction was observed. However, the presence of Sb on the surface inhibited the formation of 7×7 reconstruction. The Sb cell temperature was regulated at 300 °C, which corresponds to a deposition rate of 0.1 pm/s on substrates held at room temperature (no Sb desorption expected). The Sb coverage corresponding to the RHEED patterns in Figs. 2(b) and 2(c) was not sufficient for the SME growth of the Ge desired.

In order to form proper Schottky contacts between Ge and Cr, Sb doping of the Ge film has to be minimized. It has been shown that by increasing the substrate temperature Sb segregation is strongly enhanced and therefore the Sb doping is reduced.[10] We found that depositing the first Sb monolayer at 600 °C and then raising the temperature was instrumental in obtaining sufficient Sb coverage for SME growth even at 710 °C. The RHEED pattern shown in Fig. 1(b) was obtained using this process.

B. Germanium film characterization

In Fig. 3 a cross-sectional transmission electron micrograph (TEM) of a film grown at 700 °C is shown. Stress induced contrast is visible at the Si–Ge interface, where the mismatch induced stress is relieved by a dislocation network. The interface is smooth. In the left part of the image a threading dislocation can be seen. From plane view TEM pictures a threading dislocation density of 10^8-10^9 cm^{-2} was measured. The crystalline quality of the films was further studied by Rutherford backscattering spectrometry/channeling (RBS/C). For all substrate temperatures mini-

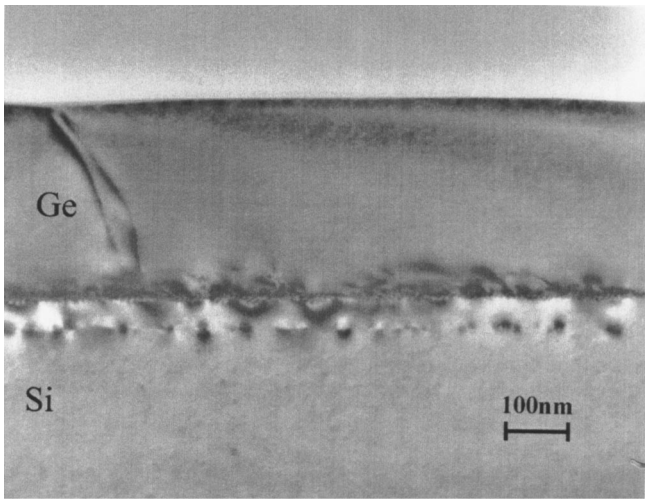

FIG. 3. Cross-sectional transmission electron micrograph of a Ge film grown at 700 °C by surfactant mediated epitaxy using Sb.

mum yields of 5% for axial channeling and 22% for planar channeling were found. A typical spectrum is depicted in Fig. 4. Good channeling is observed in the Ge film, and strong dechanneling occurs at the Ge/Si interface due to the dislocation network. Atomic force microscopy (AFM) measurements confirmed that the surface of the films was flat. The typical root mean square (rms) roughness of our layers is 0.8 nm.

Electrical transport measurements were performed at room temperature in van der Pauw geometry. We found an increase in the specific resistivity over more than three orders of magnitude when the growth temperature was increased from 600 to 710 °C (Fig. 5). This reflects the lower dopant concentration in the films due to enhanced Sb segregation at higher temperature. The squares in Fig. 5 represent films of high crystalline quality, the cycle is measured for a film of lower quality. In this case the Sb coverage was not sufficient

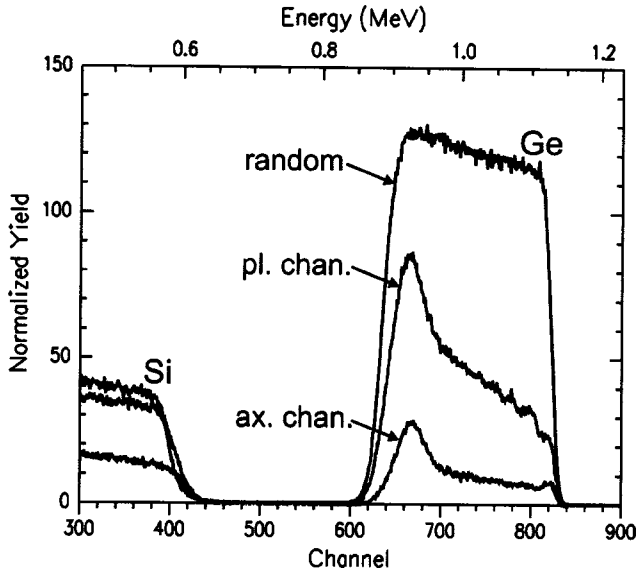

FIG. 4. Rutherford backscattering/channeling spectra of the Ge film grown at 700 °C. The spectra were measured with He^+ ions of 1.4 MeV under normal incidence and a backscattering angle of 170°.

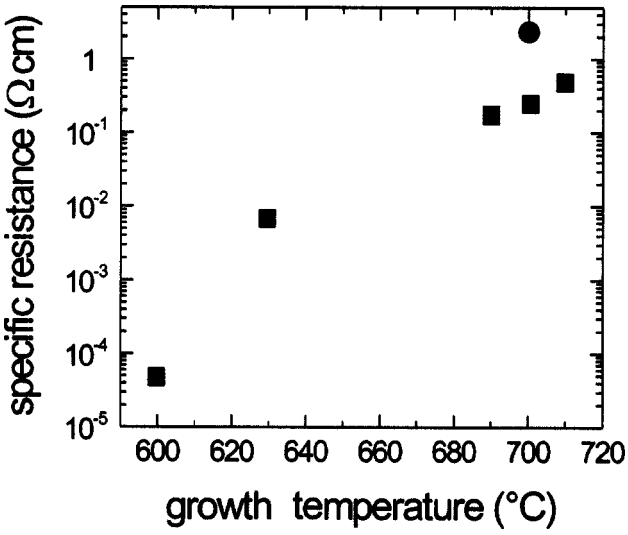

FIG. 5. Dependence of the specific resistivity of the Ge films (measured at room temperature) as a function of the growth temperature. The measurements were performed in van der Pauw geometry.

for SME growth. The axial channeling yield of this layer was 10%, and the Ge/Si interface was rough and the threading dislocation density was about two orders of magnitude higher than that for the other samples. Therefore, we attribute its high specific resistivity to reduced mobility due to the low crystalline quality. Secondary ion mass spectroscopy (SIMS) yielded values of Sb concentration of 10^{19} cm^{-3} for the sample grown at 600 °C and of 4×10^{16} cm^{-3} for the sample grown at 700 °C. Samples grown at 700 °C were used to fabricate the detectors.

C. Device fabrication and dc measurements

The design of the MGeM photodetectors is schematically shown in Fig. 6. After MBE growth of a 300 nm Ge film the top 30 nm was etched off to remove any remaining antimony contamination from the surface. Subsequently the Ge surface was passivated by depositing 50 nm of SiO_2 by plasma enhanced chemical vapor deposition (PECVD). The passivation greatly reduces the device leakage current, and this will be discussed below.

Using standard photolithography and a wet etching process a window in the oxide layer was opened and 50 nm of Cr was deposited to form Schottky contacts. The electrical

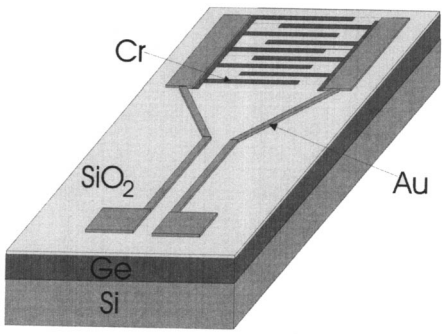

FIG. 6. Design of the MGeM photodetectors with interdigitated electrodes.

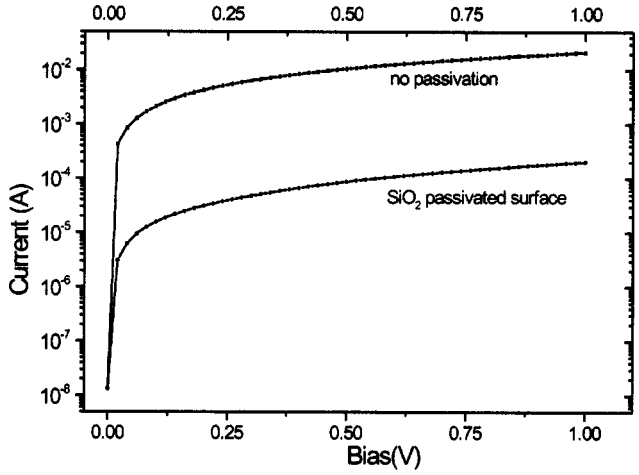

FIG. 7. Dark current characteristics of a MGeM detector with an area of 100×100 μm^2 and 3 μm finger spacing with and without SiO_2 passivation.

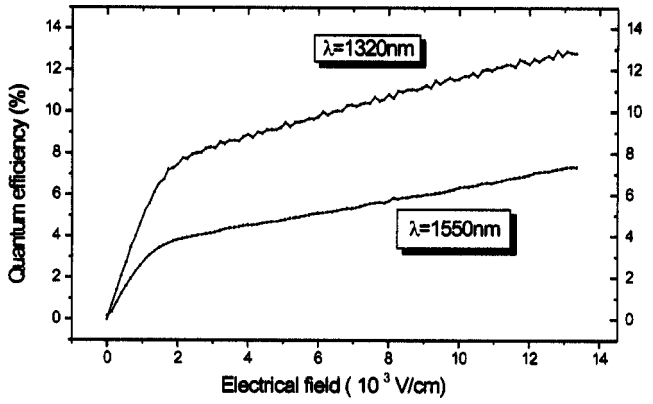

FIG. 8. Total external quantum efficiency at $\lambda=1320$ and 1550 nm vs electrical field strength for a detector with an area of 100 μm^2 and 1.5 μm electrode spacing.

contacts (the microstrip lines and the bond pads) also are realized by lithography and liftoff using 20 nm Cr and 200 nm Au for metallization.

The interdigitated detector area has a quadratic size ranging from 10×10 to 100×100 μm^2, with fingers 1.5, 2, 3, and 5 μm in width equally separated. The capacitance of the interdigitated electrode structure is in the range of 1–10 fF, depending on the finger separation and width. The coplanar microstrip line wave impedance is 60 Ω.

In the detector region oxide deposition passivates the germanium surface and reduces the surface current. This is shown by dark current measurements on a large detector (100×100 μm^2, 3 μm spacing) with and without SiO_2 passivation; see Fig. 7. The passivation improves the dark current by two orders of magnitude.

Two laser diodes at 1320 and 1550 nm were used for the dc photocurrent measurements. Light from optical fibers in vertical incidence is coupled into the detectors on a micropositioning stage. The dark current and the photocurrent were measured under identical conditions.

The total external quantum efficiency at 1320 and 1550 nm versus electrical field strength for a detector with an area of 100 μm^2 and 1.5 μm electrode spacing is presented in Fig. 8.

The photoresponse increases rapidly if an electrical field is applied. For fields exceeding 1.3×10^4 V/cm overall quantum efficiencies of 13% and 7.5% at wavelengths of 1320 and 1550 nm, respectively, were measured. These overall efficiencies correspond to responsivities of 140 and 90 mA/W, respectively.

Considering the reflection losses at the germanium surface and those from the Cr electrodes (~50% coverage), the internal quantum efficiencies calculated are 35% for 1320 nm and 22% for 1550 nm.

These values are found to be almost constant for optical input powers from 100 μW to 1 mW. This shows the linearity of the detectors as a function of input power for values below 1 mW.

D. Time response measurements

1. Experimental setup

The time response of the photodiodes was analyzed by femtosecond spectroscopy. For wavelengths of 700–900 nm, a Ti:sapphire laser provides pump and probe pulses of 150 fs full width at half maximum (FWHM). The Ti:sapphire laser also pumps an additional optical parametric oscillator, which generates IR optical pulses. The average power of the pulses impinging on the detector is 1 mW. The resulting electrical signal propagates along the Cr/Au microstrip line and is probed by a second laser pulse that passes through an electro-optical $LiTaO_3$ crystal. The crystal is positioned on top of the Au line close to the detector in order to minimize any signal dispersion due to propagation along the microstrip lines. An adjustable optical delay line allows measurements on a time scale up to 120 ps. A schematic of the setup is given in Ref. 5. Note, that electro-optic sampling permits excellent resolution of electrical device performance in the time domain, but the observed signal to noise ratio is limited by the sensitivity of the setup using an external $LiTaO_3$ probe positioned on top of the electrical lines. The electrical signal available at the input of an additional electrical preamplifier is best estimated from the results presented in the previous paragraph.

2. Optimum performance results

As examples of our best devices, detectors with an active area of 100–400 μm^2 were analyzed. No signal could be detected at 0 V bias, because the symmetrical structure does not provide built-in potential.

Figure 9 shows the fastest response measured at wavelengths of 1300 and 1550 nm. The temporal response is essentially identical, while the electrical signal amplitude is higher at 1300 nm due to the higher quantum efficiency. The effective absorption depth is limited to the Ge film thickness and is identical for both wavelengths. The temporal response is a consequence of the carrier dynamics in the Ge film only. For a given electrode spacing L, the average carrier travel distance is $L/2$ and the average transit time τ is $\tau=0.5\times L/v_s$, where v_s is the carrier saturation drift velocity. For an electrode spacing of 1.5 μm this leads to $\tau=12.5$ ps,

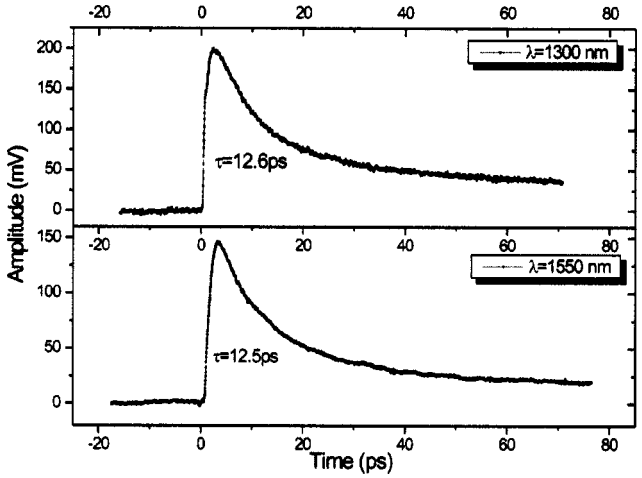

FIG. 9. Electrical response from a MGeM detector with 1.5 μm electrode spacing at $\lambda=1300$ (a) and 1550 nm (b). Bias voltage applied $U=4$ V; optical power $P_{opt}=1$ mW.

which is in perfect agreement with the observed result. The pulse width, measured in the time domain, corresponds to a -3 dB bandwidth of $f_{3\,dB}=1/2\pi\tau_t\sim 13$ GHz.

3. Influence of the electrical field

Carrier acceleration within the Ge is a function of the external field applied, which depends on the electrode spacing and the voltage applied. Carrier dynamics control the pulse response. The pulse shape as a function of applied voltage can be seen in Fig. 10. The excitation wavelength was 1550 nm. The signal was obtained from a detector with an area of 10×10 μm^2 and 1.5 μm electrode spacing.

The shape of the pulse is characterized by the following features: (1) a very fast rise time, (2) fast decay corresponding to carrier sweep out, and (3) a subsequently slower tail.

The rising part of the signal is due to the instantaneously induced current in the external circuit. This current stems from charges moving inside the volume of the detector. It is limited by the carriers effective mass, the speed attained, and by a *RC* time constant, which includes the influence of the electrodes and of the external microstrip lines.

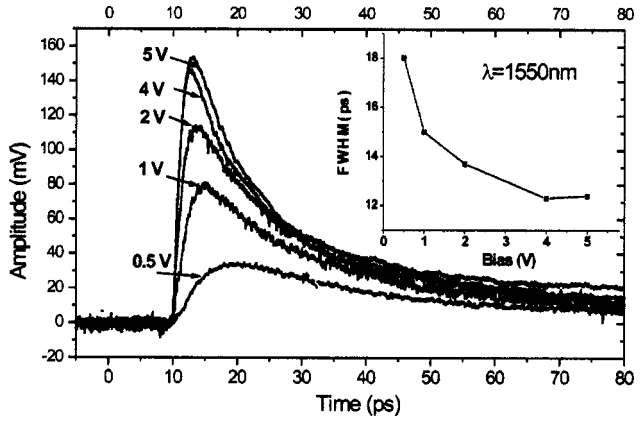

FIG. 10. Electrical response for different applied voltages from a MGeM detector with 1.5 μm electrode spacing. The measured FWHM is shown in the inset. Optical power $P_{opt}=1$ mW.

TABLE I. Comparison of the measured response times with calculated values for electron and hole drift times for different electrode separations and applied bias voltages. The last line gives the best result obtained for the interdigitated detectors.

Voltage applied (V)	Electrode spacing (μm)	Theoretical drift time for electrons (ps)	Theoretical drift time for holes (ps)	Measured FWHM (ps)
1	1.5	12.5	17.4	15.1
1	2	16.6	25	22.6
1	3	25.8	42.8	29.2
3	3	25	30	27.3
7	3	25	25	25.2
4	1.5	12.5	12.5	12.6

The decreasing part of the signal represents the rapid sweepout of the carriers from the Ge layer.

Due to the low capacitance of our photodetectors, signal decay is not influenced by the *RC* time constant. As a consequence, the FWHM of the signal is primarily determined by carrier dynamics. Its field dependence is a consequence of carrier acceleration.

The total current j is the sum of the electrons' and holes' contribution: $j=j_e+j_h$. In Ge, electrons reach saturation drift velocity v_s at an electrical field of $E=3\times 10^3$ V/cm and holes at $E=2\times 10^4$ V/cm.[11] At applied bias of 1 V ($E=6\times 10^3$ V/cm), the electrons move towards the anode with saturation drift velocity, and the holes attain a lower speed. The drift velocity of the holes increases with the field strength up to $E=2\times 10^4$ V/cm, until 4 V ($E=2.4\times 10^4$ V/cm) where the detector operates in the saturation regime, which gives the fastest response. Higher voltages are no longer advantageous.

In addition, the influence of electron and hole dynamics on the total current is observed by changing the electrode separation at constant applied bias. Table I shows the measured response times and a comparison with calculated values for electron (e) and hole (h) drift.[11] For 3 μm electrode spacing and low voltage the holes are much slower than the electrons. In this case, the fast signal is generated mostly by the electrons.

The tail of the signal is ascribed to trapping and detrapping, especially at interfaces and defects, which act as carrier traps.

4. Response to very high illumination power

Due to the submicrometer thickness of the Ge film and the correspondingly small sensitive Ge volume of order 100 μm^3, the detectors have a limited range of linearity for high illumination powers. If the power of the incident light pulses is increased from 1 to 10 mW, a decrease in the response speed and nonlinear distortion of the pulse shape is observed; see Fig. 11. Figure 11 shows the impulse response from a detector with 2 μm electrode spacing. At 1 mW power, an estimated density of 10^{17} e–h pairs/cm^3 is expected. At higher optical intensities an increase in carrier density leads to an increase in carrier recombination, screening of the electrical field from the electrodes applied, and a change in the

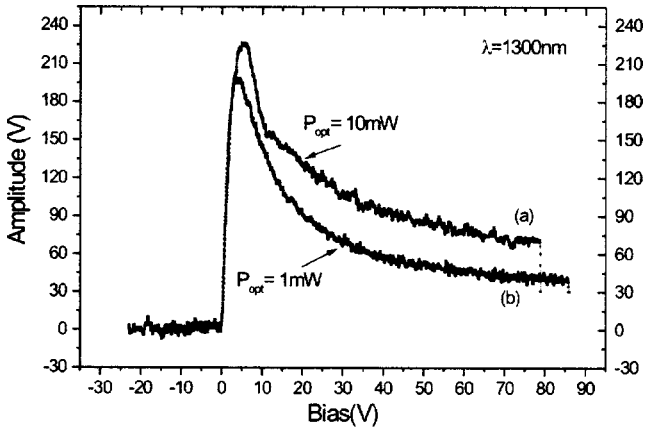

FIG. 11. Electrical response from a MGeM detector with 2 μm electrode spacing at $\lambda = 1300$ nm for different incident optical powers: input optical power P_{opt} = (a)10 and 1 mW (b).

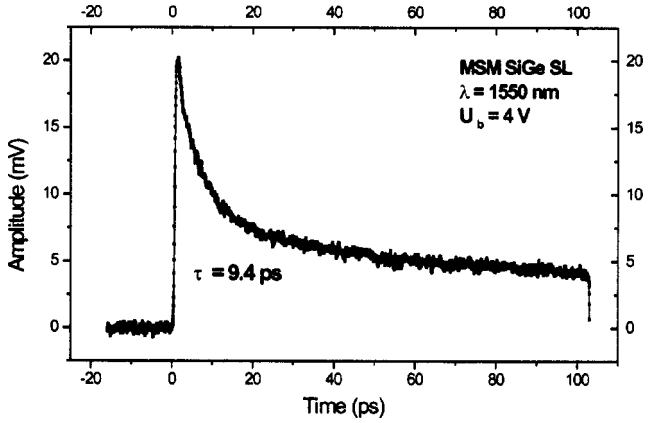

FIG. 12. Electrical response from a plate capacitor type SiGe superlattice detector at $\lambda = 1550$ nm. The SiGe layer thickness is 340 nm.

reflectivity of the Ge film. The results presented for high power (Fig. 11) are not a limitation to possible applications, since these signal powers are excessive.

E. Comparison to a SiGe undulating superlattice detector

We have extended the IR femtosecond response measurements to MSM detectors with vertical ''plate capacitor'' electrodes. An important difference between the interdigitated design, discussed earlier, and the vertical plate capacitor is the absence of low electrical field regions below interdigitated electrodes. In a plate capacitor, the thickness of the semiconductor film between the electrodes directly defines the carrier drift length. It is not limited by the resolution of the lithography, as in the case of the fingers, and it can be grown as thin as desired. Typically, vertical MSM detectors use epitaxial $CoSi_2$ buried metal electrodes. If Si can be used as the photosensitive layer, the Cr/Si/$CoSi_2$ heterostructure provides excellent performance in ultrafast MSM devices.[12] It was attempted to replace the Si by Ge. Therefore Ge was grown on top of the $CoSi_2$ layer using the same SME technique explained earlier and good crystalline quality was achieved.[13] Nevertheless, the MSM plate capacitor detectors with Ge as the intended active layer suffered from additional problems during Ge epitaxy on $CoSi_2$ and good Schottky barriers with low dark currents could not be obtained.

In contrast, MSM SiGe undulating layer superlattice detectors were fabricated using an epitaxial $CoSi_2$ layer on Si(100) as the bottom electrode.[14] The Si–SiGe superlattice was grown by MBE and had an average Ge content of 45 at. % per layer. It has been shown that metastable $Si–Si_{0.5}Ge_{0.5}$ strained undulating superlattices exhibit optical transition energy of 0.8 eV, corresponding to a wavelength of 1550 nm.[15] A semitransparent Cr film (8 nm) served as the top electrode. This results in a capacitor structure with 340 nm Si–SiGe–Si between the electrodes and a capacitance of approximately 300 fF.

The *RC* time constant of the detector is $\tau_{RC} = 3.2$ ps. The response from a detector with an area of 700 μm^2 at a pump wavelength of 1550 nm is shown in Fig. 12. The measured FWHM is 9.4 ps. The corresponding -3 dB bandwidth amounts to $f_{3\,dB} = 17$ GHz. At a wavelength of 1550 nm the overall quantum efficiency of this detector is 0.9%.

In contrast to the interdigitated design, the speed of the vertical MSM device is limited by the *RC* time constant of the detector. The trailing edge of the signal is a convolution between sweepout of the carriers and the *RC* time constant of the detector. As a consequence, the device is fastest at a certain detector thickness, typically in the range of 300–500 nm. Any further decrease in detector thickness will not improve the device speed, because the gain in speed by reduction of the carrier drift length is overcompensated by an increase of the *RC* time constant.[5]

III. SUMMARY

We have fabricated silicon-based MSM photodetectors for near infrared optocommunication wavelengths, $\lambda = 1300–1550$ nm, and evaluated them by femtosecond spectroscopy and electro-optical sampling. Two different designs were demonstrated.

(1) A photosensitive epitaxial Ge film of 270 nm thickness, grown by surfactant mediated epitaxy on Si(111). In this case interdigitated top Cr electrodes were used as electrical contacts and they provided good Schottky barriers. The speed of these detectors is determined by the drift time of the photogenerated electrons and holes to the Cr fingers. For finger spacing of 1.5 μm an electrical pulse width of 12.5 ps FWHM is measured for both wavelengths, 1300 and 1550 nm. The overall quantum efficiency is 13% at 1320 nm and it drops to 7.5% at 1550 nm.

(2) A plate capacitor design with a buried epitaxial $CoSi_2$ layer on Si(100) as the bottom electrode. In this case a MBE-grown Si–SiGe superlattice with 45% Ge in the layers was realized. These strained SiGe superlattices (SLs) are photosensitive at 1550 nm as well. The 340 nm thick SL was sandwiches between the $CoSi_2$ bottom electrode and a semitransparent Cr top electrode. Due to the shorter carrier drift length, these devices are even

faster, with a pulse response of 9.4 ps FWHM at 1550 nm, but have a lower overall quantum efficiency of 0.9%.

Both designs show record response times for any silicon-based ultrafast detectors at infrared wavelengths (1300–1550 nm).

Details of the temporal evolution of the response current were analyzed as a function of the voltage applied, electrode spacing, wavelength, and illumination intensity. The usable bandwidth was found to exceed 10 GHz. Excessive illumination intensity of 10 mW reduces this value. At low illumination intensity, quantitative agreement between the experimental results and the theoretically expected carrier dynamics was found.

ACKNOWLEDGMENT

The authors thank the European Union for financial support (EU-LTR project No. 31838 ''SCOOP'').

[1] H. Zimmermann, *Integrated Silicon Optoelectronics* (Springer, Berlin, 2000).
[2] C. Moglestue, J. Rosenzweig, J. Kuhl, M. Klingenstein, A. Axmann, Jo. Schneider, and A. Hülsmann, J. Appl. Phys. **70**, 2435 (1991).
[3] S. Y. Chou and Y. Liu, Appl. Phys. Lett. **61**, 1760 (1992).
[4] L. Colace, G. Masini, and G. Assanto, Appl. Phys. Lett. **76**, 1231 (2000).
[5] Ch. Buchal, M. Löken, Th. Lipinsky, L. Kappius, and S. Mantl, J. Vac. Sci. Technol. A **18**, 630 (2000).
[6] L. Colace, G. Masini, F. Galluzzi, and G. Assanto, J. Vac. Sci. Technol. B **17**, 465 (1999).
[7] D. Reinking, M. Kammler, M. Horn-von Hoegen, and K. R. Hofmann, Appl. Phys. Lett. **71**, 924 (1997).
[8] D. J. Eaglesham and M. Cerullo, Appl. Phys. Lett. **58**, 2276 (1991).
[9] M. Horn-von Hoegen, F. K. Le Goues, M. Copel, M. C. Reuter, and R. M. Tromp, Phys. Rev. Lett. **67**, 1130 (1991).
[10] M. Horn-von Hoegen, J. Falta, M. Copel, and R. M. Tromp, Appl. Phys. Lett. **66**, 487 (1995).
[11] S. M. Sze, *Physics of Semiconductor Devices*, 2nd ed. (Wiley, New York, 1981).
[12] M. Löken, L. Kappius, S. Mantl, and Ch. Buchal, Electron. Lett. **34**, 1027 (1998).
[13] S. Winnerl, L. Kappius, D. Buca, St. Lenk, Ch. Buchal, and S. Mantl, Microelectron. Eng. **60**, 191 (2002).
[14] S. Winnerl, D. Buca, S. Lenk, Ch. Buchal, and D.-X. Xu, Mater. Sci. Eng., B **89**, 73 (2002).
[15] D. Buca, S. Winnerl, S. Lenk, Ch. Buchal, and D.-X. Xu, Appl. Phys. Lett. **80**, 4172 (2002).